Available online at www.sciencedirect.com

ScienceDirect

Geochimica et Cosmochimica Acta 145 (2014) 268–280

Geochimica et Cosmochimica Acta

www.elsevier.com/locate/gca

# Termination and hydration of forsteritic olivine (0 1 0) surface

Hongping Yan [a,*,1], Changyong Park [a,*], Gun Ahn [b], Seungbum Hong [b], Denis T. Keane [c], Curtis Kenney-Benson [a], Paul Chow [a], Yuming Xiao [a], Guoyin Shen [a]

[a] HPCAT, Geophysical Laboratory, Carnegie Institution of Washington, Argonne, IL 60439, USA
[b] Materials Science Division, Argonne National Laboratory, Argonne, IL 60439, USA
[c] Department of Materials Science and Engineering, Northwestern University, Evanston, IL 60208, USA

Received 19 March 2014; accepted in revised form 1 September 2014; Available online 16 September 2014

**Abstract**

Termination and hydration of the forsteritic (Fo90Fa10) olivine (0 1 0) surface have been investigated with high-resolution specular X-ray reflectivity and Atomic Force Microscopy. The surface was prepared by polishing a naturally grown {0 1 0} face, from which we found the polished surface in acidic (pH 3.5) alumina suspension exhibits regular steps while the basic (pH 9.5) silica polished surface is irregularly roughened, indicating there are two distinguishable mechanochemical processes for the surface dissolution. The quantitative interpretation of the regular steps from the alumina-polished surface suggests that the observed step heights correspond to multiples of crystallographic unit cell. Only this atomically terraced surface is investigated with the high-resolution X-ray reflectivity (HRXR) to determine the surface termination and hydration. The basic silica paste polished surface turned out too rough to measure with X-ray reflectivity. HRXR reveals that the alumina polished olivine (0 1 0) surface in pure water is terminated at a plane including half-occupied metal ion sites (M1), an oxygen vacancy site, and a silicate tetrahedral unit with one of its apices pointing outward with respect to the surface. An ideal termination with the oxygen vacancy would fulfill the stoichiometry of the formula unit; however, in the observation, the vacancy site is filled by an adsorbed water species and about a quarter of the remaining metal ions are further depleted. The terminating plane generates two distinct atomic layers in the laterally averaged electron density profile, on which two highly ordered adsorbed water layers are formed. The first layer formation is likely through the direct interaction with the M1 plane and the second layer is likely through the hydrogen bonding interaction with the first water layer. With this multilayered adsorbed water structure, the surface metal ion is partially hydrated by the vacancy-filling water species and adsorbed water molecules. The bulk water links to these distinct adsorbed water layers, with weak density oscillations that almost completely damp out after the first bulk water layer. The total thickness of the layered water structure including the two distinct adsorbed layers and the first layer of bulk water is slightly less than 1 nm, which corresponds to roughly three molecular layers of water. These results describe the steric constraints of the surface metal ion hydration and the iron redox environment during water–olivine interactions in this particular crystallographic orientation.


* Corresponding authors at: HPCAT, Geophysical Laboratory, Carnegie Institution of Washington, 9700 South Cass Avenue, 434E, Argonne, IL 60439, USA. Tel.: +1 630 252 0477.
*E-mail addresses:* hyan@carnegiescience.edu, hongping.yan@northwestern.edu (H. Yan), cpark@carnegiescience.edu (C. Park).
[1] Current contacts: Center for Hierarchical Materials Design, Northwestern University, 9700 South Cass Avenue, 437D, Argonne, IL 60439, USA.

http://dx.doi.org/10.1016/j.gca.2014.09.005
0016-7037/

## INTRODUCTION

Hydrous alteration of magnesium- and iron-enriched minerals, or serpentinization of ultramafic rock, is attributed to a key thermodynamic process which can abiotically generate hydrogen and hydrocarbons in an aqueous environment (McCollom and Seewald, 2013). This process is believed to be the source of abiotic hydrocarbons found in the hydrothermal fluids in ultramafic lithologies in submarine and subaerial hydrothermal vent systems (Charlou et al., 1997, 2002). These products have been considered to provide the energy that supports the chemolithoautotrophic microorganism communities in surface and subsurface environments within both continental and seafloor settings (Alt and Shanks, 1998). They have also been considered to be the source of prebiotic organic compounds leading to the precursor form of life (Martin and Russell, 2007; Russell, 2007).

The serpentinization of mantle rocks has significant geophysical importance for the global marine system, especially for subduction zone environments. During the hydration process of oceanic ultramafic mantle rocks, the mass density of the rocks decreases, accompanied by a change in rheology, resulting in distinct differences in the physical properties of the mantle before and after the reaction, which can induce an uplift force in the mantle that is able to significantly alter the tectonic environment of the seismically active region (Früh-Green et al., 2004).

The abiotic hydrocarbon generation usually involves hydrothermal alteration of minerals during which reducing conditions are created by dissolution and reaction of ferrous iron ($Fe^{2+}$) in water, along with reduction of dissolved carbon dioxide ($CO_2$). A typical reaction is usually described such that olivine ($Mg_{2-x}Fe_xSiO_4$) reacts with water ($H_2O$), yielding the products of serpentine ($Mg_3Si_2O_5(OH)_4$), brucite ($Mg(OH)_2$), magnetite ($Fe_3O_4$), and hydrogen ($H_2$) (McCollom and Bach, 2009). The hydrogen produced in this process then further reduces the aqueous $CO_2$, which produces methane ($CH_4$) and other hydrocarbons ($C_nH_{2n+2}$). The rate of hydrogen generation is critical in understanding how significantly this abiotic process contributes to the energy sources for microbial communities in the deep-sea environment as well as to hydrocarbon generation. It is apparent that the generation rates and the total yield of final reduction products highly rely on both the dissolution rates of olivine that provides $Fe^{2+}$ and partitioning of the dissolved $Fe^{2+}$ into the product minerals, for example, magnetite ($Fe_3O_4$). The importance of iron speciation is obvious as the rate determining process because the iron redox process is directly involved in the water reduction that generates molecular hydrogen.

The rate and mechanism of olivine dissolution have been widely studied under various physical and chemical conditions, such as ionic strength, pH, temperature and even organic ligands (Wogelius and Walther, 1991; Chen and Brantley, 2000; Pokrovsky and Schott, 2000b; Oelkers, 2001; Hänchen et al., 2006). For example, the kinetics and mechanism of forsterite (Mg-bearing end-member of olivine) dissolution at 25 °C and pH from 1 to 12 has been studied (Pokrovsky and Schott, 2000b), where two distinguishing dissolution mechanisms were suggested for acidic and weakly alkaline solutions and stronger alkaline (pH >9) solutions. Rimstidt et al. (2012) developed rate equations of forsterite dissolution in solutions with pH ranging from 0 to 14 and temperature from 0 to 150 °C. They pointed out that the olivine surface is not homogeneously reactive but the concentration of reacting sites and/or the reactivity differs along different crystallographic orientations.

Computational methods have also been extensively employed to understand the stability of both the pure and the hydrated forsterite surfaces. The use of atomistic simulations was demonstrated for the evaluation of the structure of mineral surfaces and provided simulated data for pure forsterite surfaces (Watson et al., 1997). De Leeuw et al. (2000) used atomistic simulations to investigate stability of various forsterite surfaces and the hydration of these surfaces. The feasibility of chemisorption of water molecules onto forsterite dust grains of various crystallographic surfaces has been tested by computations and considered as the possible source of water for rocky planets (King et al., 2010). Most recently, the First-Principles Density Functional Theory was employed to examine the adsorption mechanisms of water on a variety of forsterite low-index surfaces, concluding that water dissociation was the preferred mode of adsorption of water molecules for the (100), (010) and (110) surfaces (Asaduzzaman et al., 2013).

Notwithstanding these significant experimental and computational works, there is no experimentally determined structural data available so far to be directly compared to the atomistic models and the interpretations in molecular scale. In this study, we probe the pristine hydration structure at the olivine (010)–water interface experimentally. We measure the high-resolution X-ray reflectivity (HRXR) from a single crystal olivine (Fo90Fa10) surface immersed in deionized (DI) water in the specular reflection geometry and derive the electron density profile in the surface normal direction, representing the atomistic perspective of interfacial hydration and water ordering. The method has been successfully applied for probing interfacial hydration structures of a number of mineral surfaces with various crystallographic orientations (e.g., alumina (001) (Eng et al., 2000); barite (001) and (210) (Cheng et al., 2001); muscovite (001) (Cheng et al., 2001); quartz (101) and (100) (Schlegel et al., 2002); orthoclase (001) and (010) (Fenter et al., 2003a); fluorapatite (100) (Park et al., 2004); alumina (012) (Catalano et al., 2006); hematite (012) and (110) (Catalano et al., 2007); and goethite (100) (Ghose et al., 2010). We combine the HRXR technique with ex-situ Atomic Force Microscopy (AFM) measurements to characterize the surface morphologies that vary for different sample polishing conditions. The derived electron density profile at the olivine (010)–water interface is interpreted in terms of the atomistic configuration of partial hydration of surface metals and water ordering at the interface. The detailed interfacial hydration structure is discussed in the context of energetically stable surface termination and metal hydration.

## 2. MATERIALS AND METHODS

The single crystal forsteritic olivine samples used in this study are naturally grown ones from Sapat, Naran, in Pakistan. The chemical composition has been reported previously: $Mg_{1.807}Fe_{0.178}Ni_{0.007}Mn_{0.003}Ca_{0.001}Si_{1.002}O_4$ (Gose et al., 2008). The lattice parameters are $a = 4.764$ Å, $b = 10.227$ Å, and $c = 5.995$ Å in an orthorhombic system (McCormick et al., 1987). Its crystal structure is represented by a ball-and-stick model with silica tetrahedra in Fig. 1A. Along the surface normal direction, [0 1 0], the unit cell

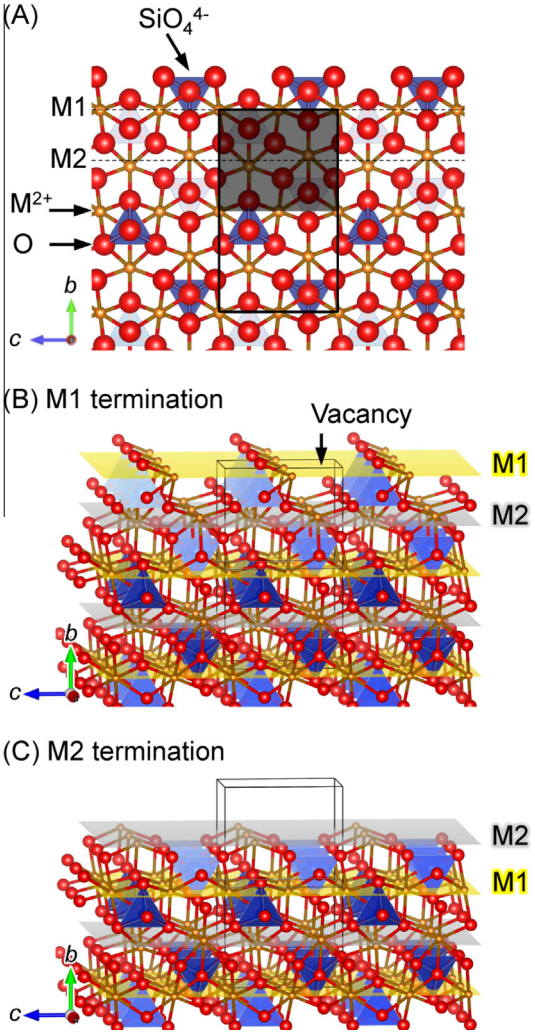


Fig. 1. Crystal structure of olivine viewed along the *a*-axis (A), stoichiometric surface termination M1 (B) and M2 (C), with M1 and M2 color-coded. A unit cell of the crystal is indicated in (A) by a rectangle centered in the figure (solid line). Smaller spheres represent metal ions, either $Mg^{2+}$ (90%) or $Fe^{2+}$ (10%), and larger spheres represent oxygen atoms. Si atoms are not visible in the figure, but their positions are indicated by the silicate tetrahedra. Dashed lines show two potential termination planes of (0 1 0) surface centered on virtual planes containing the two metal sites, "M1" and "M2", respectively. The grey-shaded rectangle indicates the physical unit cell in [0 1 0] direction, which is a half of the original unit cell. The (0 1 0) diffraction is forbidden because of this translational symmetry in the unit cell.

*d*-spacing reduces to a half of the original unit cell for the translational symmetry, resulting in $d_{0\,1\,0} = 5.1135$ Å (shown with shaded area in Fig. 1A) instead of the original 10.227 Å (shown with solid line in Fig. 1A), thus hereafter the term "unit cell" refers to this physical unit cell. As illustrated in Fig. 1A within a unit cell, the metal atoms define two distinguishing planes where relatively few metal–oxygen bonds need to be broken when the surface is terminated: one at a fractional height of 0 with two metal ions strictly in a plane (denoted as plane "M1" in Fig. 1), and the other at a fractional height of ½ with two metal ions alternating positions around the plane (denoted as plane "M2" in Fig. 1).

The mineral specimen exposes a large {0 1 0} face, which is considered to be the most stable surface under dissociated water hydration according to earlier atomistic simulation (de Leeuw et al., 2000). Two small pieces (with dimensions of millimeters) of sample with (0 1 0) single crystal surface were cut from this specimen and were polished using a lapping machine. In order to investigate the effect of sample preparation on the quality of polished surface, two polishing strategies were employed, with the aim of obtaining an atomically flat surface required for HRXR experiments: Sample No. 1 was polished with 3 μm alumina colloidal particles suspended in pH = 3.5 aqueous solution for 8 h, followed by 1 μm and 0.3 μm alumina particles for 8 h each, and a final touch with 0.03 μm colloidal alumina suspension (Allied, pH = 3.5) for 24 h; Sample No. 2 was polished with 0.3 μm silica particles in ethanol for 8 h, followed by 0.1 μm silica particles for 8 h and a final touch with 0.05 μm colloidal silica aqueous suspension (Allied, pH = 9.5) for 24 h. The polished samples were then cleaned ultrasonically in DI water for 5 min and stored in clean and dry containers. Before mounting the samples for reflectivity experiments, each sample was cleaned again ultrasonically in acetone, methanol and DI water for 15 min each successively to remove possible organic contaminants.

The cleaned sample was then mounted in a thin-film cell (Fenter, 2002) as depicted in Fig. 2. The sample was covered and held in place by an 8-μm thick Kapton film on a plastic (PEEK) cell base. The cell was inflated by very slowly flowing DI water to fully wet the surface and then gently drained with gravitational forces to allow the capillary force between the mineral surface and the Kapton film to form a thin water film (less than a few tens of microns) for the X-ray measurement. The cell was closed during the X-ray measurement with no water flowing through

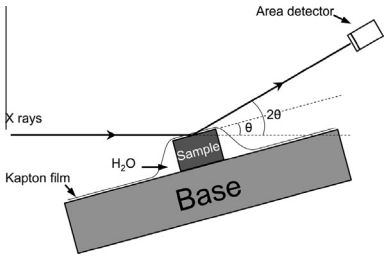


Fig. 2. Schematic of the thin film cell and the experiment geometry of X-ray reflection.

the cell. It is possible that minute contents of carbonate species may be accumulated in the cell by dissolving atmospheric $CO_2$ permeated through the thin Kapton polyimide film during the X-ray measurement. However, we did not observe the direct effect on our X-ray data, perhaps due to either sensitivity limit or negligible contents.

The high-resolution specular X-ray reflectivity measurements were performed at beamline 5-IDC of Advanced Photon Source (APS), Argonne National Laboratory (ANL) (Walko et al., 2004). This measurement basically scans the (00$L$) crystal truncation rod (CTR) intensities along the surface normal direction in $\theta$–$2\theta$ scan geometry (Fenter, 2002; Fenter and Sturchio, 2004). The intensity obtained in this geometry is sensitive to the average depth profile of the electron density and, most importantly, to the interfacial atomic structure where the water molecules interact with the sample surface. The full description of the method can be found in a review article by Fenter (2002). Because the sample surface polished with silica particles in basic solution (Sample No. 2) exhibits relatively larger roughness that diminishes the reflectivity intensities in between Bragg peaks, the reflectivity analysis focuses only on data acquired on sample surface polished with alumina particles in acidic condition (Sample No. 1).

An X-ray beam with the energy of 17.460 keV and spot size 100 μm horizontally and 30 μm vertically was used for the specular X-ray reflectivity measurement. The high incident flux of $2 \times 10^{11}$ photons/s sufficed for the large dynamic range of reflectivity variation as a function of the incident angle. A full measurement took three to four hours including the positioning of diffractometer at each data point. A Pilatus 100 K detector mounted on the diffractometer arm at a distance of 570 mm away from the sample was used to collect the reflected X-rays. The scattering area on the area detector was defined by a detector slit with the size of 5 mm vertically and 5 mm horizontally in front of the Pilatus detector. The background subtraction and the peak intensity integration were performed following the conventions described by Fenter et al. (2006). In order to reduce the background scatter from sources outside the sample, a set of guard slits with the size of 1 mm vertically and 1 mm horizontally at 250 mm away from the detector were used. The collimation focus could not be exactly the same with the beam footprint on the sample surface, but it was effective to avoid unwanted scattering from objects other than the sample.

Atomic Force Microscopy (AFM, Asylum Research MFP3D, Santa Barbara, CA) was used to examine the surface quality of the samples after polishing, specifically the surface morphology and roughness. The AFM was operated in contact mode to ensure atomic level resolution in surface height measurements. Image processing details are described in the results and discussion section.

## 3. RESULTS AND DISCUSSION

### 3.1. High-resolution X-ray reflectivity

The measured specular X-ray reflectivity intensities from the polished mirror-like olivine (0 1 0)–water interface as a function of momentum transfer, $q = (4\pi/\lambda)\sin\theta$, are presented in Fig. 3, where $\lambda$ is the incident X-ray wavelength and $\theta$ is half of the $2\theta$ reflection angle (Fig. 2). The X-ray reflectivity measurements were performed for both Sample No.1 (alumina-polished in pH = 3.5) and Sample No. 2 (silica-polished in pH = 9.5), but only Sample No. 1 showed the features representing a homogeneous, single terminated surface. Therefore, the high-resolution reflectivity data and the corresponding interfacial profile discussed hereafter are all based on the result of Sample No. 1. The intensities were normalized by an incident beam monitor. The errors were propagated from the counting statistics and convoluted with the systematic error that was derived by evaluating the fiducial measurements at $L = 0.95$ during the data acquisition. Within a $q$ range from 0.25 to 6.48 Å$^{-1}$ the data shows six mid-zone intensity regions between and beyond Bragg peaks at reciprocal lattice units of $L = 1$, $L = 2$, $L = 3$, $L = 4$ and $L = 5$, respectively, where $L = 1$ corresponds to (0 2 0) Bragg peak.

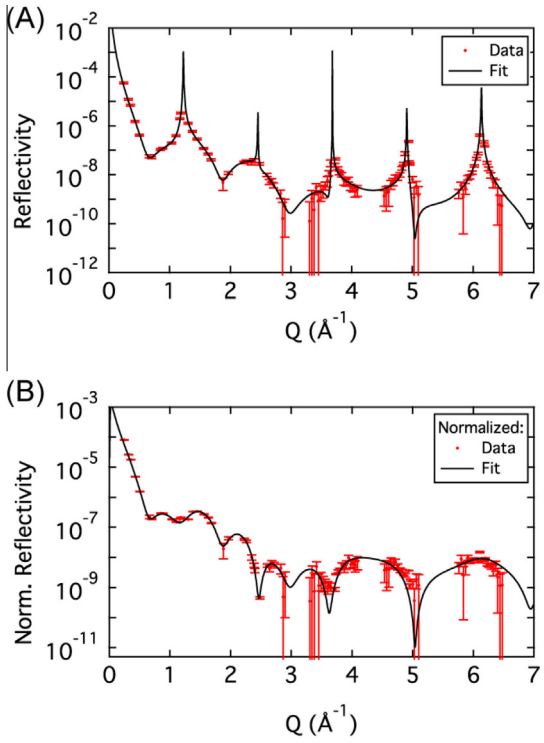


Fig. 3. (A) Reflectivity data (markers with error bars) and the best fit (solid line) for olivine (0 1 0) (Sample No. 1)–water interface; and (B) data and the best fit normalized to the crystal truncation rod intensity (i.e., $|F_{CTR}|^2$).

The measured reflectivity can be reproduced based on a structure factor model for the known crystal structure of the substrate and a few modeling strategies for the interfacial regions (Fenter and Sturchio, 2004):

$$I(q) \propto |F_{\text{sub.uc}}F_{\text{CTR}} + F_{\text{interface}} + F_{\text{water}}|^2 \quad (1)$$

Although the structure factor model (Eq. (1)) consists of three mathematical terms, it represents four major physical components forming the mineral–water interface: (1) semi-infinite single crystal, (2) the surface unit cells which deviate

to any extent from the bulk, e.g., relaxation in the *d*-spacing, depletion, etc., (3) adsorbed water, and (4) semi-infinite bulk water. In Eq. (1), $F_{\text{sub.uc}}F_{\text{CTR}}$ corresponds to component (1), $F_{\text{interface}}$ includes both (2) and (3), and $F_{\text{water}}$ represents component (4). The intensities measured at the mid-zone regions between Bragg peaks are more sensitive to the interfacial structure, while the near-Bragg regions are more influenced by the single crystal substrate. As the near-Bragg intensities are more constrained by the known substrate structure than the unknown mid-zone regions, they are crucial in establishing self-consistent intensity references to estimate the absolute reflectivity throughout the entire *q*-range. In that sense, while our data suffer from a partial lack of interface-sensitive mid-zone intensities in higher *q* regions (Fig. 3), the frequent appearance of the near-Bragg regions allows us to estimate the model structures even with the partially limited data.

Since *q* is reciprocal of the real space *d*-spacing through the relation $q = 2\pi/d$, the spatial resolution is related to the maximum *q* that can be approached experimentally. The maximum *q* value of 6.48 $\text{Å}^{-1}$ in our data provides with an effective spatial resolution of $\pi/q = 0.48$ Å, assuming that the electron density profile for each scattering atom can be modeled by a Gaussian distribution and its full-width at the half-maximum (FWHM) defines the spatial resolution. The $\pi/q = 0.48$ Å experimental resolution corresponds to the root-mean-square (rms) width of a Gaussian with $\sigma = 0.20$ Å, which is to be convoluted when the total electron density profile is presented.

### 3.2. Termination of hydrated olivine (0 1 0) surface

It is predicted by previous atomistic calculation (de Leeuw et al., 2000) that the forsterite (0 1 0) surface terminated with a smooth plane of O–Mg–O (non-dipolar termination M2, stoichiometry plane shown in Fig. 1C) is most stable under unhydrated conditions, which is possibly due to the formation of the O–Mg–O bridges lowering the energy of the surface. This termination is also more stable over M1 (dipolar termination, stoichiometry plane shown in Fig. 1B) under associative hydration. In contrast, the M1 termination with a half-vacant magnesium plane becomes the most stable when the surface is hydrated with dissociated water molecules (hydroxylation of the surface), according to the simulation with a monolayer of dissociated water. The hydroxyl groups of the dissociated water molecules are strongly bonded to the remaining surface magnesium ions, and their hydrogen atoms, together with the hydrogens bonded to lattice oxygen, tilt towards the magnesium vacancies to balance the surface charges created by magnesium depletion. Furthermore, the hydrated M1 termination is still more stable with associative adsorption of another layer of water molecules. It also revealed that during the dissolution of forsterite, in terms of the chemical exchange processes, replacing a magnesium ion by two hydrogen ions for M1 termination is energetically more favorable than that for M2 termination.

Based on these computational predictions, we calculated the X-ray reflectivity for the two potential terminations (M1 and M2 planes) and compared the results to the measured data. The results are shown in Fig. 4 with clearly better agreement for calculated X-ray reflectivity with M1 termination near the first Bragg peak. In this comparison, no adsorbed or bulk water was included, and no refinement for the interfacial structures was executed because the near-Bragg-peak intensities are sufficient for determining the termination. The result is consistent with the atomistic simulation proposing the M1 plane termination under dissociative hydration conditions (de Leeuw et al., 2000). Note that the physical unit cell of the olivine (0 1 0) crystal (Fig. 1A) is composed of two sub-unit cells in mirror symmetry about the M2 plane. According to the "termination interference" description in Ref. (Fenter and Park, 2004), this termination corresponds to "Type I", which discriminates the two possible terminations in an unequivocal way due to the distinct X-ray phase effect. The M1 plane termination was further verified by the fact that the full parameter fitting did not converge to any physically feasible model structure when refining the structures with the other termination (a graphical demonstration is not shown here to avoid redundancy).

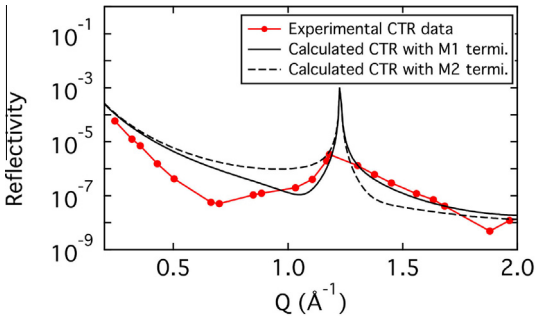


Fig. 4. Plots showing comparison between the calculated crystal truncation rod (without water) from olivine (0 1 0) surface with two different terminations and experimental data (line with markers) around the first Bragg peak. CTR calculated with M1 termination (solid line) shows better agreement than that with M2 termination (dashed line).

### 3.3. Hydration at the olivine (0 1 0)–water interface

We performed a least-squares fitting analysis to refine the interfacial atomic structures terminated with the M1 plane. A few assumptions were made for the initial input, especially for the physical constraints caused by the M1 plane termination. Firstly, a pair of metal ions and a silicate tetrahedral unit must be removed from the terminating plane (Fig. 1B) to fulfill the stoichiometry of the formula unit. The consequence is that the oxygen atom at fractional position 0.8953, which was originally a part of the tetrahedron, and a metal atom at 1.0000 are removed, leaving behind vacancy sites (labeled in Fig. 1B). Secondly, because breaking up the $SiO_4$ units leads to less stable surfaces (Davies, 1992) and metal ions are preferentially released at pH less than 8.5 (Oelkers et al., 2009), the remaining silicate tetrahedron units are presumed to be intact with an oxygen atom poking out of the M1 plane at fractional position 1.1047. However, the occupancy for the remaining

metal ions, $Occ_1$, is taken as a parameter for refinement as it could be further depleted. In such cases, it is speculated that the depleted surface charge must be neutralized by adsorbed water species or re-adsorbed metal species. Thirdly, the dissociated water species (e.g., hydroxyl ion) will be able to take the place of the vacancy site and their occupancies and positions need to be determined, as $Occ_2$ and $z_2$, respectively. Finally, as commonly expected for an abruptly truncated single crystal surface, relaxation of the surface atom positions is expected to minimize the surface energy. With expected adsorption of water species, these relaxed atomic positions must be determined. These factors are parameterized in the least-squares fitting using the equations, especially the first term of Eq. (7), $F_{\text{interface}}$, described in the Appendix.

For the adsorbed water on top of this terminating plane, the positions, distribution widths, and occupancies ($z_{H2O}$, $\sigma_{H2O}$, and $N_{H2O}$, respectively) are to be determined. The true structure of adsorbed water layers, however, is completely unknown in the initial structure factor modeling; therefore, the final structure for the best-fit model must be found through a trial-and-error approach. In our analysis, two layers of adsorbed water on top of the terminating plane were found to best reproduce the measured reflectivity data. Besides these adsorbed water layers, the transition water structure connecting the interfacial water to bulk water is assumed to consist of a layered bulk water structure (Fenter, 2002). The occupancy and the layer spacing of the layered bulk water are pre-characterized with fixed numbers, i.e., 2.8 per surface unit cell area of $a_{uc} = 28.5602$ Å$^2$ and a uniform layer spacing of $c_{w,bulk} = 2.99$ Å, based on the known constraint of the bulk water density, 1 g/cm$^3$, at room temperature and pressure. However, the first layer position of $z_{H2O,bulk}$, the Debye–Waller like width, $\sigma_{0,bulk}$, and the average distribution width of the water layers, $\sigma_{bar,bulk}$, which depicts the distribution width $\sigma_{n,bulk}$ of the $n$th layer of water molecules with the equation $\sigma_{n,bulk} = (\sigma^2_{0,bulk} + n\sigma^2_{bar,bulk})^{1/2}$, must be optimized during the fit (Eq. (8) in the Appendix). This layered bulk water model is employed due to its flexibility in representing both layer-featured and featureless bulk water models simultaneously by adjusting the constraint on the model parameters. Because we found the total thickness of the bulk water film plus the Kapton film, $D_w$, interferes with the scale factors during the fit, and $D_w$ will affect reflectivity through the X-ray attenuation factor only at low-$q$, we constrain it to be 18 μm, which is an 8 μm Kapton film plus a 10 μm water film on top of the sample surface. The roughness of the sample surface is modeled by Robinson's $\beta$ parameter, which is related to the rms roughness by the equation $\sigma_{rms} = d_{010}\beta^{1/2}/(1-\beta)$, with $d_{010}$ being the $d$-spacing along the [0 1 0] direction (Robinson, 1986). These parameters and their values from the best-fit model are summarized in Table 1.

During the fitting process, the parameters describing the occupancy of the M1 plane atoms ($Occ_1$) and the position and the occupancy of the space-filling species ($Occ_2$, $z_2$) exhibit high covariance behavior. Therefore, as a work-around method to evaluate the uncertainties of positions and occupancies of the M1 plane atoms and the space-filling species, we fit parameters for these two layers of atoms individually, meaning that we first optimize $Occ_2$ and $z_2$ when $Occ_1$ is fixed, and then optimize $Occ_1$ when $Occ_2$ and $z_2$ are fixed. Final uncertainties are taken to be whichever value is greater for each of these parameters respectively, to ensure a higher likelihood of real values falling into the uncertainty intervals.

Table 1
Parameters derived from the best-fit model.

| Parameters | Values from best-fit | Standard error | Units |
|---|---|---|---|
| $\beta$ | 0.134 | 0.024 | – |
| $z_{H2O,1}$ | 1.559 | 0.048 | Å |
| $N_{H2O,1}$ | 2.894 | 0.313 | – |
| $\sigma_{H2O,1}$ | 0.692 | 0.084 | Å |
| $z_{H2O,2}$ | 3.581 | 0.056 | Å |
| $N_{H2O,2}$ | 3.386 | 0.237 | – |
| $\sigma_{H2O,2}$ | 0.704 | 0.040 | Å |
| $z_{H2O,bulk}$ | 6.581 | 0.060 | Å |
| $\sigma_{0,bulk}$ | 1.042 | 0.038 | Å |
| $\sigma_{bar,bulk}$ | 0.990 | 0.131 | Å |
| $Occ_1$ | 0.497 | 0.067 | – |
| $Occ_2$ | 1.178 | 0.087 | – |
| $z_2$ | −0.166 | 0.024 | Å |
| $\Delta y$ | −0.188 | 0.038 | Å |
| S | 6.328 | 0.174 | – |

$\beta$: Robinson's roughness parameter; $z_{H2O,1}$: position of the first adsorbed water layer; $N_{H2O,1}$: occupancy per surface unit cell of the first adsorbed water; $\sigma_{H2O,1}$: position distribution width of the first adsorbed water layer; $z_{H2O,2}$: position of the second adsorbed water layer; $N_{H2O,2}$: occupancy per surface unit cell area ($a_{uc}$) of the second adsorbed water layer; $\sigma_{H2O,2}$: position vibrational amplitude of the second adsorbed water; $z_{H2O,bulk}$: position of the first layer of bulk water; $\sigma_{0,bulk}$: Debye–Waller like amplitude for the first layer of bulk water; $\sigma_{bar,bulk}$: parameter specifying how quickly the vibrational amplitude increases for each water layer into the bulk; $Occ_1$: occupancy of Mg at the very top surface M1 positions; $Occ_2$: occupancy of the vacancy filling water estimated as oxygen equivalent at the M1 plane; $z_2$: position of oxygen equivalent water at the surface; $\Delta y$: relaxation of the surface $SiO_4^{4-}$ unit; $S$: scale factor.

The best fit of the reflectivity data is plotted in Fig. 3 with solid lines. The fit curve reproduces the data well overall, except for several data points where the experimental signal–noise-ratio is low. The chi-square (defined as $\chi^2 = \sum(I_i - I'_i)^2/\sigma_i^2/(N-P)$, where $I_i$ is the $i$th calculated reflectivity intensity, $I'_i$ the measured intensity, $\sigma_i$ the error of measured value, $N$ the number of data points, and $P$ the number of parameters to fit, respectively) for this least-squares fitting is 5.923. This chi-square value, which is far larger than unity, indicates that the structure factor model may still need more parameters to fully reproduce all the details of the measured reflectivity or there are some unrecognizable errors in the measured data; however, we accept the current result as a minimal set of structural components to represent the key features of the interfacial structure.

Based on the best-fit model, the electron density profile near the interfacial region can be derived. The ball and stick model in Fig. 5A presents the atomic structures representing the best fit result, together with the corresponding electron density profile plotted in Fig. 5B. Since the

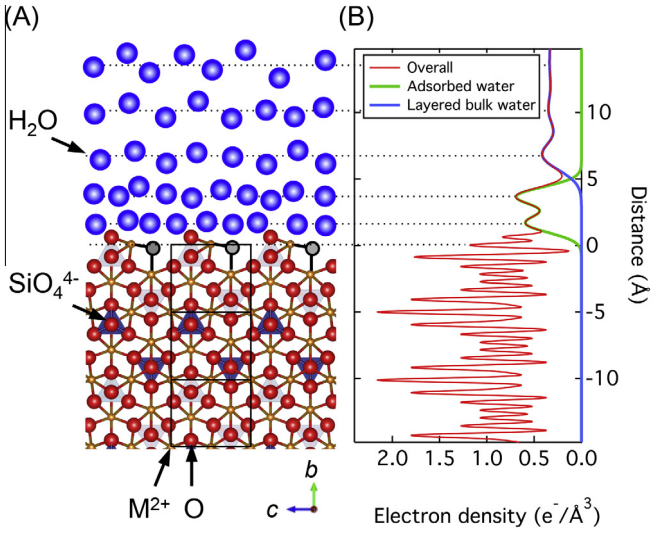


Fig. 5. (A) Ball and stick model of the olivine (0 1 0)–water interface inferred from the electron density profile derived from the best fit result, which is plotted in (B). The electron density profile is the laterally averaged one-dimensional projection along the surface normal direction that is calculated from the best-fit model. The substrate structure is viewed in *a*-axis. Three unit cells in the surface region are indicated in the scheme by rectangles with solid outlines. Outlined circles filled with a shaded pattern at the surface (close to 0 Å position) represent the possible vacancy-filling water species that bond to the under-coordinated $M^{2+}$ ions.

specular X-ray reflectivity method retrieves only information along the surface normal direction, this profile shows the laterally averaged one-dimensional electron density profile.

The fit converges to a model indicating that the metal occupancy at the fractional height 1 of the unit cells (at the very top crystal surface) decreases from 1 to $0.497 \pm 0.067$. The model contains atoms with an oxygen-equivalent occupancy of $1.178 \pm 0.087$ at the fractional position of $0.968 \pm 0.005$, which is 0.166 Å lower than the M1 plane (fractional position = 1). Around the M1 termination plane, the compositional variation between the metal ions (including the remaining $Mg^{2+}$ or $Fe^{2+}$) and the adsorbed water species are completely indistinguishable, because the monochromatic X-rays are not sensitive enough to discriminate them. However, it is reasonable to assume that some of the metal ions at the original fractional position 1 relaxed into this slightly lower position. Assuming that all the remaining metal ions after depletion are bonded to oxygen atoms of species from dissociated water (shown in Fig. 5A with circles and black bold-solid lines), it can be calculated that the space-filling species are equivalent to $0.752 \pm 0.060$ oxygen atoms and $0.255 \pm 0.053$ metal ions. This results in a total occupancy of $(0.497 + 0.255) = 0.752$ for the remaining metal ions in the surface termination plane. It corresponds to a 24.8% further depletion of the surface metals than what is expected from an ideal stoichiometric formula. The termination of the surface is in close agreement with the previous atomistic simulation (de Leeuw et al., 2000), i.e., M1 (dipolar) is more stable under dissociative hydration comparing to M2 (non-dipolar) termination, except that we observed a further depleted metal occupancy. The difference could be due to the experimental conditions including the mechanochemical polishing and the existence of bulk water following the adsorbed water species, which could not be included in the computational calculation. As indicated in de Leeuw et al.'s computations, the replacement of magnesium ions with two hydrogen ions is an energetically favorable process in acidic environment, thus we suspect that the extra depletion of metal ions is a consequence of the use of an acidic polishing solution as observed before (Oelkers et al., 2009), where a preferential release of metal ions was identified at pH less than ~8.5–10 for all investigated divalent metal silicates.

The surface metal ions are bonded to two types of oxygen atoms in the steric condition: (1) the oxygen atoms of the silicon tetrahedron and, (2) the oxygen atoms of species obtained from the dissociatively adsorbed water. Although the exact chemical species of the latter cannot be directly identified, it can be inferred that the vacancy filling species is more likely to be the hydroxyl ion ($OH^-$) rather than hydronium ion ($H_3O^+$), considering the apparent point of zero charge ($pH_{PZC}$) of the sample surface and the influence that the hydroxyl ion has on the surface. The $pH_{PZC}$ of the acid reacted forsterite surface is around 7 (Pokrovsky and Schott, 2000a), which means there are no redundant charges on the surface and all the surface charges should be balanced out in aqueous condition. The oxygen vacancies created at fractional position 0.895 due to removal of silicate tetrahedrons cause a localized excess positive charge because of the undercoordination of metal ions, and the partial depletion of metal ions cannot balance out this effect completely. As a consequence, it is easier for hydroxyl ions to approach the surface and form chemical bonds with the exposed metal ions. In addition, the tilting of the proton end of the hydrogen atoms of bonded hydroxyl ions, together with the protons adsorbed to the tetrahedron oxygen atoms, can balance the negative surface charge produced by metal ion depletion, as observed before where the tilting of hydrogen atoms balanced the charge introduced by silicon vacancy (Wright et al., 1994). However, because

the arrangement of hydrogen atoms is beyond our experimental sensitivity due to their extremely low electron density, so we could not observe this effect directly in our data.

In addition to the water species occupying the vacancy site and forming a bond to the remaining surface metal ions, the fitted model suggests two additional layers of water immediately adjacent to this terminating plane, whose electron density is shown with the green curve in Fig. 5B. These two adsorbed water layers are followed by the bulk water, as illustrated with the blue curve in Fig. 5B. A schematic view of these water molecules is presented with blue spheres in Fig. 5A, in which the fluctuation of the water molecule positions in the *b* and *c* directions reflects the randomness of the real molecular positions.

In order to derive a model structure to reflect more realistic behavior, these two adsorbed water layers are fitted completely independently with respect to their positions ($z_{H2O}$), occupancies ($N_{H2O}$) and distribution widths ($\sigma_{H2O}$). The first layer of adsorbed water molecules is located at $1.559 \pm 0.048$ Å above the M1 termination plane with occupancy of $2.894 \pm 0.313$ per surface unit cell. The second layer of adsorbed water molecules is located at $3.581 \pm 0.056$ Å with the occupancy of $3.386 \pm 0.237$ per surface unit cell. Above these two adsorbed layers, the bulk water begins at a height of $6.581 \pm 0.060$ Å, with a fixed layer spacing of 2.99 Å separating a series of Gaussian peaks (Magnussen et al., 1995), which is determined by the limit of the bulk density of water with 2.856 water molecules per one surface unit cell (28.5602 Å$^2$), equivalent to the common value of about one water molecule per 10 Å$^2$ in bulk water. This adsorption of layered water molecules on surfaces has been widely observed and reported for a variety of oxides and natural minerals (Fenter and Sturchio, 2004).

Taking into account that the M1 termination is possibly hydroxylated by dissociated water molecules, the two distinct adsorbed water layer structure can be interpreted such that the first layer of water molecules interacts with partially depleted M1 plane composed of metal ions and the vacancy-filling water species through metal–oxygen bonding (M–O) and hydrogen bonding, while the second layer of water molecules interacts with the highly-ordered first layer of adsorbed water. As indicated by the distinct layered feature, there should be substantial steric constraint in forming the hydrogen-bonding network through these adsorbed water layers. It is worth to mention that the vertical distance between the second adsorbed water layer and the apex oxygen atom layer is ~3.233 Å, which still supports the possibility of forming a weak hydrogen bonding directly between these two layers. However, the relatively dense first layer of adsorbed water will strongly constrain this interaction so that the second water layering is most likely due to strong hydrogen bonding interaction with the first adsorbed water layer. Immediately beyond these two adsorbed layers, the bulk water exhibits additional layers, which show quickly damped density fluctuations. The peak diminish within a range equivalent to about one molecular layer (~3 Å) beyond the relatively sharp first layer. This sharp first layer of bulk water seems more directly influenced by the specifically adsorbed layer (Fig. 5B, blue curve).

It is worth mentioning that the first two adsorbed layers possess an average water occupancy of $(2.894 + 3.439)/2 = 3.166$ per unit cell area, or 0.111/Å$^2$. Considering the layer spacing, the corresponding equivalent average water density for these two layers is $1.450 \pm 0.096$ g/cm$^3$, which is significantly higher than the density for bulk water at room temperature and ambient pressure. This density is also equivalent to a center-to-center distance of water molecules of 2.474 Å, in contrast to the value of ~2.8 Å for normal water density. Deviation of water-equivalent density from the ideal water density at immediately near surface region has been predicted by computational work before (Kerisit et al., 2012). However, we do not rule out the potential cause due to the incomplete fitting indicated by the large chi-square value and the possibility that these two adsorbed layers do not consist exclusively of water. Other species may be adsorbed to the crystal surface causing a deviation from the perfectly pristine hydration condition. For example, metal ions dissolved from the surface could be immediately hydrated and re-adsorbed, or aluminum residuals from the polishing process may remain on the surface as contamination. Further investigation is desired to clarify this mysteriously high-density water at the interface.

### 3.4. AFM surface morphology

The morphology of the polished olivine (0 1 0) surface was characterized by ex-situ Atomic Force Microscopy (AFM). A 1 μm by 1 μm AFM image (256 × 256 points) for the alumina polished surface and its analysis are shown in Fig. 6. The image was processed by a low-pass filter mask to obtain a noise-reduced image.

In Fig. 6A, the olivine (0 1 0) surface polished at pH = 3.5 with alumina paste (Sample No. 1) exhibits a characteristic morphology with wavy steps. The rms roughness from this AFM image is determined to be 1.107 Å, comparing to the roughness of $2.161 \pm 0.253$ Å from the above X-ray reflectivity analysis. The difference is attributed to the significantly larger sampling area for the X-ray reflectivity measurement, because the smallest beam foot print even at the highest *q* is much larger than the 1 μm by 1 μm area from AFM shown in Fig. 6A. An important feature of this morphology is the alternation of peaks and valleys in its height profile. A line profile is plotted in Fig. 6B, with the line position indicated in the image of Fig. 6A by a solid line. It is obvious that the line profile consists of peaks and minimums alternately, with an asymmetric peak shape of flat pre-peak section (left-hand side) and non-flat post-peak section (right-hand side) with an additional hump. This AFM morphology can be caused by a slight miscut of the (0 1 0) surface and the convolution with the tilt angle of the sample when mounted, which results in a surface composed of two groups of distinct surfaces: (1) the olivine (0 1 0) surface and, (2) the ledge face of the step. The spacing between the exposed (0 1 0) surfaces corresponds to the distance between these two adjacent flat sections, i.e., the distance *h* between the line AB and the line CD as illustrated in Fig. 6C. Based on this deduction, several line profiles from the AFM are evaluated. Each of the

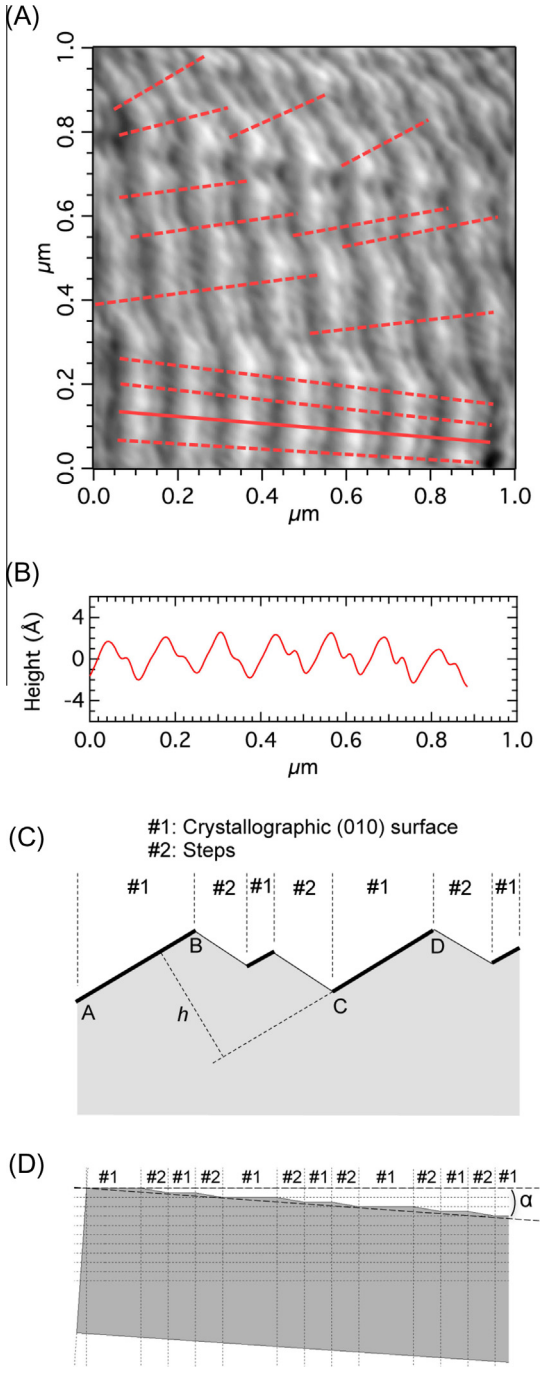


Fig. 6. AFM image of alumina-polished forsterite (010) surface (Sample No. 1) and data interpretation: (A) the height distribution with lines indicating positions where line profile analysis are sampled; (B) An example of line profiles as indicated by the solid straight line in (A); (C) schematic of proposed surface morphology corresponding to the observed AFM image; and (D) schematic showing the sample miscut which results in the surface morphology proposed in (C).

peaks is analyzed such that the pre-peak section is fitted to a straight line and the spacings between these lines are calculated as the height difference of the exposed (010) surfaces. This simple geometric derivation from the line profiles at each peak location yields an average $h$ of $9.68 \pm 1.38$ Å based on statistics of 54 topographical peaks obtained from 14 line profiles, whose positions are shown with lines in Fig. 6A. This step height is about twice the one-dimensional unit cell height along the [010] direction, 5.1135 Å. Based on this topographical analysis, a promoted scheme based on the derived information is shown in Fig. 6D. It suggests that the post-peak sub-minimums are due to the removal of unit cells to form the steps. The shaded area represents the mineral sample and the top border of the shaded area corresponds to the polished sample surface. Horizontal dashed lines with a spacing of 10.227 Å in this scheme indicate the planes of real crystallographic (010) surfaces at different heights. According to this analysis, the miscut angle is determined to be $0.48 \pm 0.07$ degrees. The AFM data further confirms that most of the exposed polished sample surface is the (010) crystallographic plane with the estimated miscut. This is consistent with our X-ray reflectivity result, which confirms a homogeneous single termination surface.

In contrast to the alumina polished surface, the AFM image of the surface after polishing with 0.05 μm silica colloidal paste in pH = 9.5 solution shows a distinct departure from a homogenous termination (Fig. 7). As shown in a line profile in Fig. 7B, the surface was randomly roughened, resulting in a morphology with a random distribution of heights that yields a root-mean-square roughness of 18.102 Å. This significantly larger roughness is possibly caused by the dissolution of silicon tetrahedrons under basic

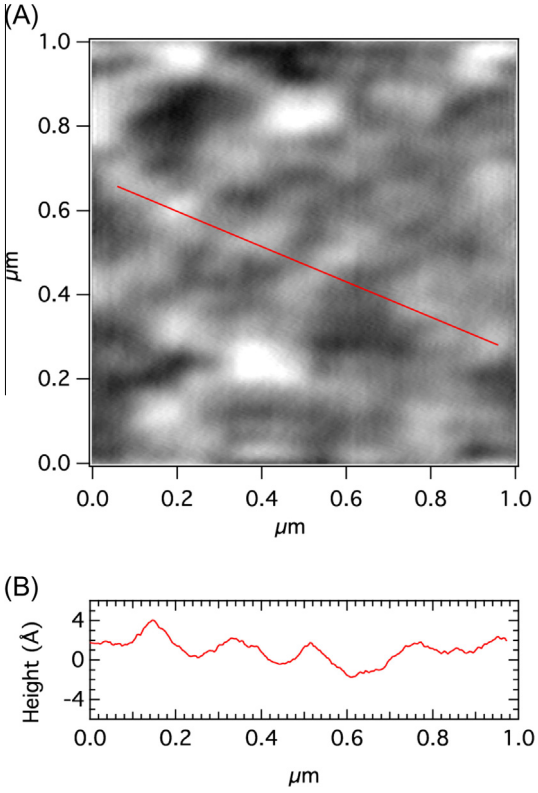


Fig. 7. (A) AFM image of silica-polished olivine (010) surface at pH = 9.5 (Sample No. 2), and (B) the line profile obtained on the line indicated in the image.

conditions, according to previously reported observations (Oelkers et al., 2009), where it is found that cation exchange reactions lead to Si-depleted surfaces at basic pH. This random roughness can cause significant reduction of the X-ray reflectivity intensity, which was confirmed during our experiment by the observation that there was almost no measurable X-ray reflectivity intensity from this surface.

The two distinct surface morphologies between the acidic alumina polished surface (Sample No. 1) and the basic silica polished surface (Sample No. 2) indicate fundamentally different reaction mechanisms for each condition. The dissolution mechanisms of mineral surfaces at various aqueous conditions have been studied in the past. For example, the dissolution mechanism of single crystal orthoclase surfaces has been investigated (Teng et al., 2001; Fenter et al., 2003b), from which two distinct reaction mechanisms could be defined: a layer-by-layer dissolution mechanism vs. an etch-pit forming mechanism. The distinction is caused by a different reactivity between the exposed surfaces to the solution, i.e., the reactivity difference between the terrace surface and the ledge surface around the step. The distinct surface morphologies shown at the olivine (0 1 0) surface after acidic and basic polishing, respectively, similarly indicate the possible existence of mechanistic differences between the crystallographic orientations.

### 3.5. Implications for olivine serpentinization

The process of hydrocarbon generation during serpentinization of mantle rocks is well studied for temperatures greater than 200 °C (Moody, 1976; Seyfried et al., 2007; McCollom and Bach, 2009). However, the mechanism of hydrogen generation from serpentinization at lower temperatures than the known limit of life, which is about 122 °C according to Takai et al. (2008), has been in debate for a long time. McCollom and Bach (2009) suggested that the thermodynamic constraints on mineral stability and on Fe-distribution among the product minerals as a function of temperature are likely to be major factors controlling the extent of $H_2$ production, which results in a negligible amount of hydrogen generated at low temperatures because of the increased partitioning of $Fe^{2+}$ into brucite. The direct experimental proof for significant hydrogen generation at temperatures below 100 °C, however, has been observed in recent laboratory studies (Neubeck et al., 2011; Mayhew et al., 2013). In these studies, the olivine surfaces were examined with micro- probing and mapping techniques to better understand the mechanism and constraints of dissolution and serpentinization of olivines at low temperatures when hydrogen generation occurs. Study of olivine surfaces introduces a catalysis effect that was proposed based on the observed correlation between the presence of secondary minerals on the olivine surface and hydrogen generation, especially at low temperatures. Secondary minerals on the surface of olivine are therefore suspected to play a significant role in the weathering process. In the work by Neubeck et al. (2011), low-temperature and long-term olivine weathering experiments confirm that $H_2$ and $CH_4$ production are probably influenced by the existence of chromite and magnetite as catalysts. Also, in the study of hydrogen generation from water reacted with ultramafic and mafic rocks at low-temperature conditions (55 and 100 °C) by Mayhew et al. (2013), a strong correlation between the presence of spinel phases, $[M^{2+}M_2^{3+}]O_4$, on the olivine surface and molecular hydrogen generation has been reported, from which it is inferred that the transfer of electrons between $Fe^{2+}$ and water at the spinel surface–water interface promotes molecular hydrogen generation. The same conclusion is further supported by an independent study revealing a water splitting process at the surface of magnetite even at room temperature (Parkinson et al., 2011). Although there is still an argument regarding background carbon source specification during laboratory simulations of abiotic hydrocarbon formation at low temperatures (McCollom, 2013), these studies still seem to suggest that the hydrogen generation is likely as a secondary process rather than as a primary product of the olivine dissolution.

The rate of hydrogen generation, however, is suggested to be proportional to the olivine dissolution rates anyway (Hellevang et al., 2011) as the source of $Fe^{2+}$ species available for the process, and is thus limited by surface related factors, such as surface area, accessibility to fresh surface, etc. More experimental investigation revealed that, during the interaction of an olivine surface with artificial seawater, the decrease of olivine dissolution caused by the presence of halite or adsorption of ions on the surface could affect the production of magnetite and hydrocarbons during serpentinization (de Souza et al., 2013). Although limited to (0 1 0) orientation, our results showing ordered water molecules adsorbed to the partially depleted $M^{2+}$ termination surface implies that the metal hydrolysis and the consequent depletion from the energetically stable surface is possibly the rate limiting factor. Furthermore, the $Fe^{2+}$ oxidation must be mediated by the hydration shell so that the formation of spinel species, involving electron transfer, is also likely regulated by the interfacial hydration. To identify the detailed reaction pathways, e.g., inner-sphere vs. outer-sphere electron transfer, further investigation of the oxidation state of the surface iron is desired.

## 4. CONCLUSIONS

In summary, the combined use of in-situ high-resolution X-ray reflectivity and ex-situ Atomic Force Microscopy revealed the interfacial hydration of olivine (0 1 0) surface immersed in bulk water to a length scale of atomic resolution and the surface morphology distinctions between acidic and basic polishing. By modeling the interfacial structure normal to the (0 1 0) surface and fitting the specular X-ray reflectivity data, we could determine the surface termination to be at the M1 plane that includes partially depleted metal ions and vacancy-filling water species. Two distinct adsorbed water layers were observed at the interface between the terminal surface and the bulk water. The highly ordered water layers near the terminal plane characterize the interfacial hydration including the partial hydration of the surface metal ions. The AFM image revealed the surface morphology of the polished olivine (0 1 0) surface,

which confirmed the homogeneous (0 1 0) termination of the surface polished by alumina under acidic conditions and the randomly roughened surface resulting from basic silica polishing. Geometric analysis of the AFM morphology showed step height distributions that correspond to multiples of the physical unit cell height.

The observed interfacial hydration at olivine (0 1 0) surface in pure water provides molecular insight into the surface metal hydration and the redox environment. The current study demonstrates previously unknown details of the interfacial hydration, especially in terms of the highly ordered water layers and the non-stoichiometric metal depletion with dissociated water filling the vacant spaces. However, further investigation will be required to identify the possible mechanistic differences between acidic and basic dissolution and the reactivity depending on the crystallographic orientations. In-situ probe of the redox state of the surface iron species remains an outstanding challenge.

## ACKNOWLEDGEMENTS

This work is a part of the Deep Carbon Observatory-Deep Energy project, supported by the Alfred P. Sloan Foundation in the United States. H. Yan is partially supported by the High-Pressure Collaborative Access Team (HPCAT). HPCAT is supported by DOE-NNSA under Award No. DE-NA0001974 and DOE-BES under Award no. DE-FG02-99ER45775, with partial instrumental funding by NSF. Portions of this work were performed at the DuPont-Northwestern-Dow Collaborative Access Team (DND-CAT) located at Sector 5 of the Advanced Photon Source (APS). DND-CAT is supported by E.I. DuPont de Nemours & Co., The Dow Chemical Company and Northwestern University. Some preliminary tests were performed at the HPCAT 16ID-D beamline through the auspices of Carnegie/DOE Alliance Center (CDAC) for the beamtime. APS is supported by DOE-BES, under Contract No. DE-AC02-06CH11357. AFM experiments conducted at Materials Science Division, Argonne National Laboratory by G. Ahn and S. Hong were supported by the U.S. Department of Energy, Office of Science, Basic Energy Sciences, Materials Sciences and Engineering Division under Contract No. DE-AC02-06CH11357.

## APPENDIX: STRUCTURE FACTOR MODELS

The parameters are incorporated into the calculations of the absolute reflectivity, $R$, with the following equations. More details about the derivations of these equations can be found in Ref. Fenter (2002). Here we only describe the equations actually used to fit the measured reflectivity data.

$$R = \left(\frac{4\pi r_e}{q a_{uc}}\right)^2 T_{cell} |B(q)|^2 |F_{sub.uc} F_{CTR} + F_{interface} + F_{water}|, \quad (2)$$

where $r_e = 2.8179\text{e}{-15}$ m is the classical electron radius. $T_{cell}$ is the thin-film cell geometry correction factor for X-ray attenuation as the function of incident angle with given thickness of water $D_w$ and X-ray attenuation length of water $\Lambda(\lambda)$:

$$T_{cell} = \exp\left(\frac{-8\pi D_w}{q\lambda\Lambda}\right) \quad (3)$$

$|B(q)|^2$ is the effect of roughness on the reflectivity as expressed with Robinson $\beta$ factor (Robinson, 1986):

$$|B(q)|^2 = \frac{(1-\beta)^2}{1+\beta^2-2\beta\cos(qd_{010})} \quad (4)$$

$F_{sub.uc}$, $F_{CTR}$, and $F_{interface}$ are described in the main text and can be calculated with the following equations:

$$F_{sub.uc} = \sum_{j}^{\text{unit cell}} Occ_j f_j \exp(iqz_j) \exp\left(-\frac{1}{2}q^2u_j^2\right), \quad (5)$$

$$F_{CTR} = \frac{1}{1-\exp(-iqd_{010})}, \quad (6)$$

$$F_{interface} = \sum_{j}^{\text{interfacial atoms}} Occ_j f_j \exp(iqz_j) \exp\left(-\frac{1}{2}q^2u_j^2\right) + f_{H2O}\exp\left(-\frac{1}{2}q^2\sigma_{H2O,1}^2\right)\exp\left(iqz_{H2O,1}\right) + f_{H2O}\exp\left(-\frac{1}{2}q^2\sigma_{H2O,2}^2\right)\exp\left(iqz_{H2O,2}\right), \quad (7)$$

$$F_{water} = f_{H2O} \times \frac{\exp\left(-\frac{1}{2}q^2\sigma_{0,bulk}^2\right)}{1-\exp\left(-\frac{1}{2}q^2\sigma_{bar,bulk}^2\right)\exp\left(iqc_{w,bulk}\right)}\exp(iqz_{H2O,bulk}) \quad (8)$$

Here, $f_{H2O}$ is the scattering factor of water, $u_j$ is the thermal vibrational amplitude of the $j$th atom. Other parameters are described in the main text for the explanation of structure model.

## REFERENCES

Alt J. C. and Shanks W. C. (1998) Sulfur in serpentinized oceanic peridotites: Serpentinization processes and microbial sulfate reduction. *J. Geophys. Res.* **103**, 9917–9929.

Asaduzzaman A. M., Laref S., Deymier P. A., Runge K., Cheng H.-P., Muralidharan K. and Drake M. J. (2013) A first-principles characterization of water adsorption on forsterite grains. *Philos. Trans. R. Soc. A* **371**, 20110582.

Catalano J. G., Park C., Zhang Z. and Fenter P. (2006) Termination and water adsorption at the γ-Al2O3 (012)-aqueous solution interface. *Langmuir* **22**, 4668–4673.

Catalano J. G., Fenter P. and Park C. (2007) Interfacial water structure on the (012) surface of hematite: Ordering and reactivity in comparison with corundum. *Geochim. Cosmochim. Acta* **71**, 5313–5324.

Charlou J. L., Donval J. P., Douville E., Radford-Knoery J., Fouquet Y., Bougault H., Jean-Baptiste P., Stievenard M., German C. and Party F. C. S. p. (1997) High methane flux between 15°N and the Azores triple junction, Mid-Atlantic Ridge: hydrothermal and serpentinization processes. *Eos Trans. Am. Geophys. Union* **78**, 83.

Charlou J. L., Donval J. P., Fouquet Y., Jean-Baptiste P. and Holm N. (2002) Geochemistry of high $H_2$ and $CH_4$ vent fluids issuing from ultramafic rocks at the Rainbow hydrothermal field (36°14′N, MAR). *Chem. Geol.* **191**, 345–359.

Chen Y. and Brantley S. L. (2000) Dissolution of forsteritic olivine at 65 °C and $2 < \text{pH} < 5$. *Chem. Geol.* **165**, 267–281.

Cheng L., Fenter P., Nagy K., Schlegel M. and Sturchio N. (2001) Molecular-scale density oscillations in water adjacent to a mica surface. *Phys. Rev. Lett.* **87**, 156103.

Davies M. J. (1992) Computer simulation of oxide surfaces and grain boundaries.

de Leeuw N. H., Parker S. C., Catlow C. R. A. and Price G. D. (2000) Modelling the effect of water on the surface structure and stability of forsterite. *Phys. Chem. Miner.* **27**, 332–341.

de Souza C. M. D., Carneiro C. E. a., Baú J. P. T., da Costa A. C. S., Ivashita F. F., Paesano A., di Mauro E., de Santana H., Holm N. G., Neubeck A., Zaia C. T. B. V. and Zaia D. a. M. (2013) Interaction of forsterite-91 with distilled water and artificial seawater: a prebiotic chemistry experiment. *Int. J. Astrobiol.* **12**, 135–143.

Eng P. J., Trainor T. P., Brown, Jr., G. E., Waychunas G. A., Newville M., Sutton S. R. and Rivers M. L. (2000) Structure of the hydrated α-$Al_2O_3$ (0001) surface. *Science* **288**, 1029–1033.

Fenter P. (2002) X-ray reflectivity as a probe of mineral-fluid interfaces: a user guide. *Rev. Mineral. Geochem.* **49**, 149–221.

Fenter P. and Sturchio N. C. (2004) Mineral–water interfacial structures revealed by synchrotron X-ray scattering. *Prog. Surf. Sci.* **77**, 171–258.

Fenter P., Cheng L., Park C., Zhang Z. and Sturchio N. C. (2003a) Structure of the orthoclase (0 0 1)- and (0 1 0)-water interfaces by high-resolution X-ray reflectivity. *Geochim. Cosmochim. Acta* **67**, 4267–4275.

Fenter P., Park C. and Cheng L. (2003b) Orthoclase dissolution kinetics probed by in situ X-ray reflectivity: effects of temperature, pH, and crystal orientation. *Geochim. Cosmochim. Acta* **67**, 197–211.

Fenter P. and Park C. (2004) Termination interference along crystal truncation rods of layered crystals. *J. Appl. Crystallogr.* **37**, 977–987.

Fenter P., Catalano J. G., Park C. and Zhang Z. (2006) On the use of CCD area detectors for high-resolution specular X-ray reflectivity. *J. Synchrotron Rad.* **13**, 293–303.

Früh-Green G. L., Connolly J. A. D., Plas A., Kelley D. S. and Grobéty B. (2004) Serpentinization of oceanic peridotites: implications for geochemical cycles and biological activity. In *The Subseafloor Biosphere at Mid-Ocean Ridges* (eds. W. S. Wilcock, E. F. Delong, D. S. Kelley, J. A. Baross and S. C. Cary) *Geophy. Monogr. Ser.*, Washington, D.C., pp. 119–136.

Ghose S. K., Waychunas G. A., Trainor T. P. and Eng P. J. (2010) Hydrated goethite (α-FeOOH) (1 0 0) interface structure: Ordered water and surface functional groups. *Geochim. Cosmochim. Acta* **74**, 1943–1953.

Gose J., Reichart P., Dollinger G. and Schmadicke E. (2008) Water in natural olivine-determined by proton–proton scattering analysis. *Am. Mineral.* **93**, 1613–1619.

Hänchen M., Prigiobbe V., Storti G., Seward T. M. and Mazzotti M. (2006) Dissolution kinetics of forsteritic olivine at 90–150 °C including effects of the presence of $CO_2$. *Geochim. Cosmochim. Acta* **70**, 4403–4416.

Hellevang H., Huang S. and Thorseth I. H. (2011) The potential for low-temperature abiotic hydrogen generation and a hydrogen-driven deep biosphere. *Astrobiology* **11**, 711–724.

Kerisit S., Weare J. H. and Felmy A. R. (2012) Structure and dynamics of forsterite-sc$CO_2$/$H_2O$ interfaces as a function of water content. *Geochim. Cosmochim. Acta* **84**, 137–151.

King H. E., Stimpfl M., Deymier P., Drake M. J., Catlow C. R. a., Putnis a. and de Leeuw N. H. (2010) Computer simulations of water interactions with low-coordinated forsterite surface sites: Implications for the origin of water in the inner solar system. *Earth. Planet. Sci. Lett.* **300**, 11–18.

Magnussen O. M., Ocko B. M. and Deutsch M. (1995) X-ray reflectivity measurements of surface layering in liquid mercury. *Phys. Rev. Lett.* **74**, 4444–4447.

Martin W. and Russell M. J. (2007) On the origin of biochemistry at an alkaline hydrothermal vent. *Philos. Trans. R. Soc. B* **362**, 1887–1925.

Mayhew L. E., Ellison E. T., McCollom T. M., Trainor T. P. and Templeton A. S. (2013) Hydrogen generation from low-temperature water–rock reactions. *Nat. Geosci.* **6**, 478–484.

McCollom T. (2013) Laboratory simulations of abiotic hydrocarbon formation in Earth's deep subsurface. *Rev. Mineral. Geochem.* **75**, 467–494.

McCollom T. M. and Bach W. (2009) Thermodynamic constraints on hydrogen generation during serpentinization of ultramafic rocks. *Geochim. Cosmochim. Acta* **73**, 856–875.

McCollom T. M. and Seewald J. S. (2013) Serpentinites, hydrogen, and life. *Elements* **9**, 129–134.

McCormick T. C., Smyth J. R. and Lofgren G. E. (1987) Site occupancies of minor elements in synthetic olivines as determined by channeling-enhanced X-ray emission. *Phys. Chem. Miner.* **14**, 368–372.

Moody J. B. (1976) Serpentinization: a review. *Litho* **9**, 125–138.

Neubeck A., Duc N. T., Bastviken D., Crill P. and Holm N. G. (2011) Formation of $H_2$ and $CH_4$ by weathering of olivine at temperatures between 30 and 70°C. *Geochem. Trans.* **12**, 6.

Oelkers E. H. (2001) An experimental study of forsterite dissolution rates as a function of temperature and aqueous Mg and Si concentrations. *Chem. Geol.* **175**, 485–494.

Oelkers E. H., Golubev S. V., Chairat C., Pokrovsky O. S. and Schott J. (2009) The surface chemistry of multi-oxide silicates. *Geochim. Cosmochim. Acta* **73**, 4617–4634.

Park C., Fenter P., Zhang Z., Cheng L. and Sturchio N. C. (2004) Structure of the fluorapatite (1 0 0)-water interface by high-resolution X-ray reflectivity. *Am. Mineral.* **89**, 1647–1654.

Parkinson G. S., Novotný Z., Jacobson P., Schmid M. and Diebold U. (2011) Room temperature water splitting at the surface of magnetite. *J. Am. Chem. Soc.* **133**, 12650–12655.

Pokrovsky O. S. and Schott J. (2000a) Forsterite surface composition in aqueous solutions: a combined potentiometric, electrokinetic, and spectroscopic approach. *Geochim. Cosmochim. Acta* **64**, 3299–3312.

Pokrovsky O. S. and Schott J. (2000b) Kinetics and mechanism of forsterite dissolution at 25°C and pH from 1 to 12. *Geochim. Cosmochim. Acta* **64**, 3313–3325.

Rimstidt J. D., Brantley S. L. and Olsen A. A. (2012) Systematic review of forsterite dissolution rate data. *Geochim. Cosmochim. Acta* **99**, 159–178.

Robinson I. (1986) Crystal truncation rods and surface roughness. *Phys. Rev. B* **33**, 3830–3836.

Russell M. J. (2007) The alkaline solution to the emergence of life: energy, entropy and early evolution. *Acta Biotheor.* **55**, 133–179.

Schlegel M. L., Nagy K. L., Fenter P. and Sturchio N. C. (2002) Structures of quartz (1 0 0)- and (1 0 1)-water interfaces determined by x-ray reflectivity and atomic force microscopy of natural growth surfaces. *Geochim. Cosmochim. Acta* **66**, 3037–3054.

Seyfried W. E., Foustoukos D. I. and Fu Q. (2007) Redox evolution and mass transfer during serpentinization: an experimental and theoretical study at 200 °C, 500bar with implications for ultramafic-hosted hydrothermal systems at Mid-Ocean Ridges. *Geochim. Cosmochim. Acta* **71**, 3872–3886.

Takai K., Nakamura K., Toki T., Tsunogai U., Miyazaki M., Miyazaki J., Hirayama H., Nakagawa S., Nunoura T. and Horikoshi K. (2008) Cell proliferation at 122 °C and isotopically heavy $CH_4$ production by a hyperthermophilic methanogen under high-pressure cultivation. *Proc. Natl. Acad. Sci. U.S.A.* **105**, 10949–10954.

Teng H. H., Fenter P., Cheng L. and Sturchio N. (2001) Resolving orthoclase dissolution processes with atomic force microscopy and X-ray reflectivity. *Geochim. Cosmochim. Acta* **65**, 3459–3474.

Walko D. A., Sakata O., Lyman P. F., Lee T. L., Tinkham B. P., Okasinski J. S., Zhang Z. and Bedzyk M. J. (2004) Surface and interface studies at APS endstation 5ID-C. In *AIP Conference Proceedings: Eighth International Conference on Synchrotron Radiation Instrumentation* (eds. T. Warwick, J. Arthur, H. A. Padmore and J. Sthör). AIP, USA, San Francisco, CA, USA, pp. 1166–1169.

Watson G. W., Oliver P. M. and Parker S. C. (1997) Computer simulation of the structure and stability of forsterite surfaces. *Phys. Chem. Miner.* **25**, 70–78.

Wogelius R. A. and Walther J. V. (1991) Olivine dissolution at 25 °C: Effects of pH, $CO_2$, and organic acids. *Geochim. Cosmochim. Acta* **55**, 943–954.

Wright K., Freer R. and Catlow C. R. A. (1994) The energetics and structure of the hydrogarnet defect in grossular: a computer simulation study. *Phys. Chem. Miner.* **20**, 500–503.

*Associate editor:* Jeffrey G. Catalano